

ARTICLE

Received 11 Dec 2012 | Accepted 26 Apr 2013 | Published 28 May 2013

DOI: 10.1038/ncomms2933

Sign-reversal of the in-plane resistivity anisotropy in hole-doped iron pnictides

E.C. Blomberg^{1,2}, M.A. Tanatar^{1,2}, R.M. Fernandes³, I.I. Mazin⁴, Bing Shen^{5,6}, Hai-Hu Wen^{5,6}, M.D. Johannes⁴, J. Schmalian⁷ & R. Prozorov^{1,2}

Unconventional superconductivity usually originates from several strongly coupled degrees of freedom, such as magnetic, charge and elastic. A highly anisotropic electronic phase, not driven by lattice degrees of freedom, has been proposed in some of these superconductors, from cuprates to iron-based compounds. In the iron pnictide BaFe_2As_2 , this nematic phase arises in the paramagnetic phase and is present for wide doping and temperature ranges. Here we probe the in-plane electronic anisotropy of electron- and hole-doped BaFe_2As_2 compounds. Unlike other materials, the resistivity anisotropy behaves very differently for electron- and hole-type dopants and even changes sign on the hole-doped side. This behaviour is explained by Fermi surface reconstruction in the magnetic phase and spin-fluctuation scattering in the paramagnetic phase. This unique transport anisotropy unveils the primary role played by magnetic scattering, demonstrating the close connection between magnetism, nematicity and unconventional superconductivity.

¹The Ames Laboratory, Ames, Iowa 50011, USA. ²Department of Physics and Astronomy, Iowa State University, Ames, Iowa 50011, USA. ³School of Physics and Astronomy, University of Minnesota, Minneapolis, Minnesota 55455, USA. ⁴Naval Research Laboratory, Code 6390, Washington, District of Columbia 20375, USA. ⁵Institute of Physics, Chinese Academy of Sciences, Beijing 100190, China. ⁶National Laboratory of Solid State Microstructures and Department of Physics, Nanjing University, Nanjing 210093, China. ⁷Institute for Theory of Condensed Matter Physics and Center for Functional Nanostructures, Karlsruhe Institute of Technology, 76131 Karlsruhe, Germany. Correspondence and requests for materials should be addressed to R.P. (email: prozorov@iastate.edu).

Two decades of intense research have shown that unconventional superconductors, including those with particularly high critical temperatures, T_c , often neighbour antiferromagnetic phases. It is believed that while long-range magnetic order is detrimental to superconductivity, magnetic fluctuations can be instrumental in assisting to form the Cooper pairs. In iron-based superconductors, proximity to stripe-type magnetic order is particularly prominent, and these two phases even coexist in some compounds. Interestingly, the transition to the long-range magnetically ordered phase is preceded or accompanied by a structural transition (see Paglione and Greene¹, and Johnston² for review). In the family of $A\text{Fe}_2\text{As}_2$ ($A = \text{Ca}, \text{Sr}, \text{Ba}, \text{Eu}$) compounds, the stripe magnetic order below T_N breaks tetragonal symmetry³, with in-plane ordering vectors $(\pi, 0)$ or $(0, \pi)$. The structural transition at $T_S \geq T_N$ preempts the magnetic one and reduces the tetragonal symmetry of the lattice to orthorhombic. It has been suggested by several experiments^{4–7} and theories^{8–12} that the tetragonal symmetry breaking is caused by magnetic, that is, electronic, rather than elastic degrees of freedom, giving rise to the so-called electronic nematic phase¹³. In a broader context, electronic nematicity has been experimentally observed in many systems such as semiconductor heterostructures¹⁴, ruthenates¹⁵, cuprate¹⁶ and iron pnictide⁴ superconductors. In BaFe_2As_2 , doping with either electrons (by Co-substitution of Fe, $\text{Ba}(\text{Fe}_{1-x}\text{Co}_x)_2\text{As}_2$) or holes (by K-substitution of Ba, $(\text{Ba}_{1-x}\text{K}_x)\text{Fe}_2\text{As}_2$) suppresses both magnetic and nematic orders, revealing superconductivity with a maximum T_c close to the edges of the magnetic/nematic dome (Fig. 1).

Below T_S , the sample splits into structural twin domains with different directions of the orthorhombic a_0 and b_0 axes ($a_0 > b_0$) (ref. 17). Applying a small uniaxial strain not only stabilizes one particular domain below T_S , but also extends the nematic phase to temperatures well above T_S , due to the coupling between the strain field and nematic fluctuations (red area in Fig. 1) (refs 7,18,19). In these strained samples, the nematic state anisotropy reveals itself not only in the small orthorhombic distortion $a_0 - b_0 \ll a_0 + b_0$, but, more so, in a pronounced anisotropy of the in-plane electrical resistivity $\rho \equiv \rho_b/\rho_a - 1$ (refs 20–22). Regardless of the microscopic nature of the nematic order parameter, ϕ , symmetry imposes that close to the nematic transition temperature, $\rho = \kappa\phi$, where κ is a coupling parameter. Indeed, this relation was verified experimentally in the parent compound of BaFe_2As_2 (ref. 18). Not surprisingly, in the only system where the electronic anisotropy was systematically studied across the nematic dome, the ruthenate $\text{Sr}_3\text{Ru}_2\text{O}_7$ (ref. 15), ρ was found to retain the same sign across the phase diagram. In the quantum Hall system of Cooper *et al.*¹⁴, on the other hand, the resistivity anisotropy was found to change sign for a particular direction of the external symmetry-breaking field, a behaviour that remains without clear microscopic interpretation.

In the BaFe_2As_2 family, most of the studies on its nematicity have focused on the electron-doped compounds, finding $\rho > 0$ in both magnetic and nematic phases^{20,21,23}. More recently, experiments in under-doped $(\text{Ba}_{1-x}\text{K}_x)\text{Fe}_2\text{As}_2$ found a rather small, but still positive, value of ρ ²².

Here we report that for larger K-doping levels, not explored in the previous studies, the anisotropy ρ changes sign both near T_S (nematic phase) and at very low temperatures (magnetically ordered phase). As the sign of ϕ is fixed by the small applied uniaxial strain, the coupling parameter κ must change sign across the magnetic/nematic dome. We interpret this sign-change as a result of asymmetric changes in the magnetic scattering and in the magnetically reconstructed band structure for electron- and hole-doping. This unique complexity of the nematic dome observed in the iron pnictides, suggests that spin-scattering

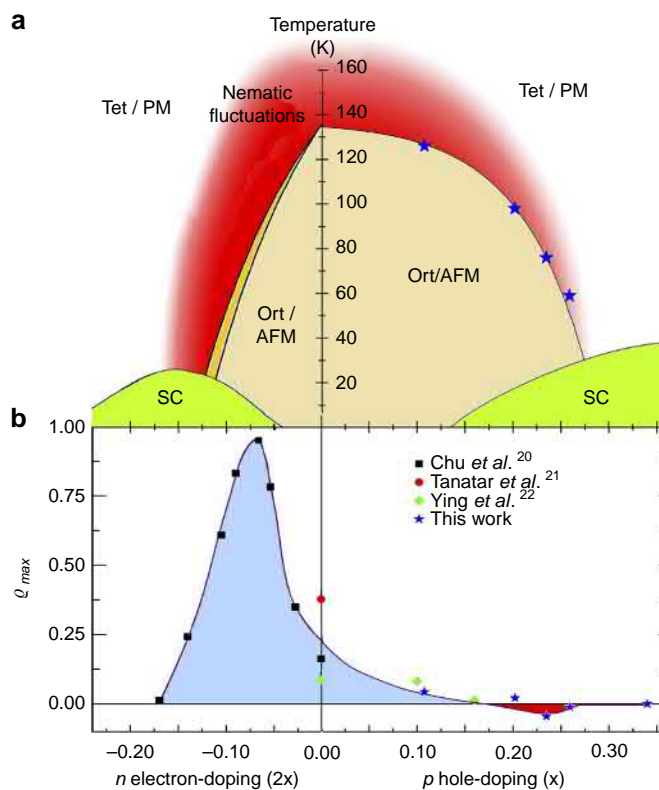


Figure 1 | Doping phase diagram and resistivity anisotropy. (a) Phase diagram of the electron- and hole-doped Ba122 system focusing on the under-doped regime with the superconducting (SC) region shown in green. The yellow region denotes the orthorhombic/antiferromagnetic (Ort/AFM) phase below the transition from tetragonal/paramagnetic (Tet/PM) phase at T_S . Nematic fluctuations (red region) persist far above T_S and affect the in-plane resistivity anisotropy in strained samples. (b) The maximum in-plane anisotropy ρ_{\max} as a function of doping. Note the significant asymmetry of $\rho_{\max}(x)$ and its sign-change in the hole-doped regime.

dominates transport in the normal state, establishing a possible connection to a magnetically mediated mechanism of superconductivity.

Results

Sign-change of resistivity anisotropy. Figure 2 presents our main experimental finding, the sign-reversal of the in-plane resistivity anisotropy. For $(\text{Ba}_{1-x}\text{K}_x)\text{Fe}_2\text{As}_2$ samples with $x \leq 0.202$, the resistivity is larger along the shorter orthorhombic axis, $\rho_a < \rho_b$, whereas for samples with $x \geq 0.235$, the longer axis has higher resistivity, $\rho_a > \rho_b$. This is clearly seen in the inset zooming in on the structural transition region. It is also apparent that, because of the applied uniaxial strain, the in-plane anisotropy starts to appear well above the structural transition T_S of the unstrained sample.

In Fig. 2b, we plot the temperature-dependent anisotropy ratio, ρ , for several compositions. We use two characteristic features of the $\rho(T)$ curves to further analyse the data. First, we plot in Fig. 1b the maximum in-plane anisotropy ρ_{\max} for different x . In Fig. 3a we plot $\rho(T \approx T_N)$, that is, at temperatures immediately below the magnetic transition, which coincides with the structural transition temperature of the unstrained $(\text{Ba}_{1-x}\text{K}_x)\text{Fe}_2\text{As}_2$ samples.

This sign-change happens at all temperatures, even near T_N , as shown in Fig. 2b and in Fig. 3a. Furthermore, as it can be seen in Fig. 2b, the magnitude of the temperature-dependent anisotropy ratio, $\rho(T)$, is maximal close to T_N in the parent and slightly hole-

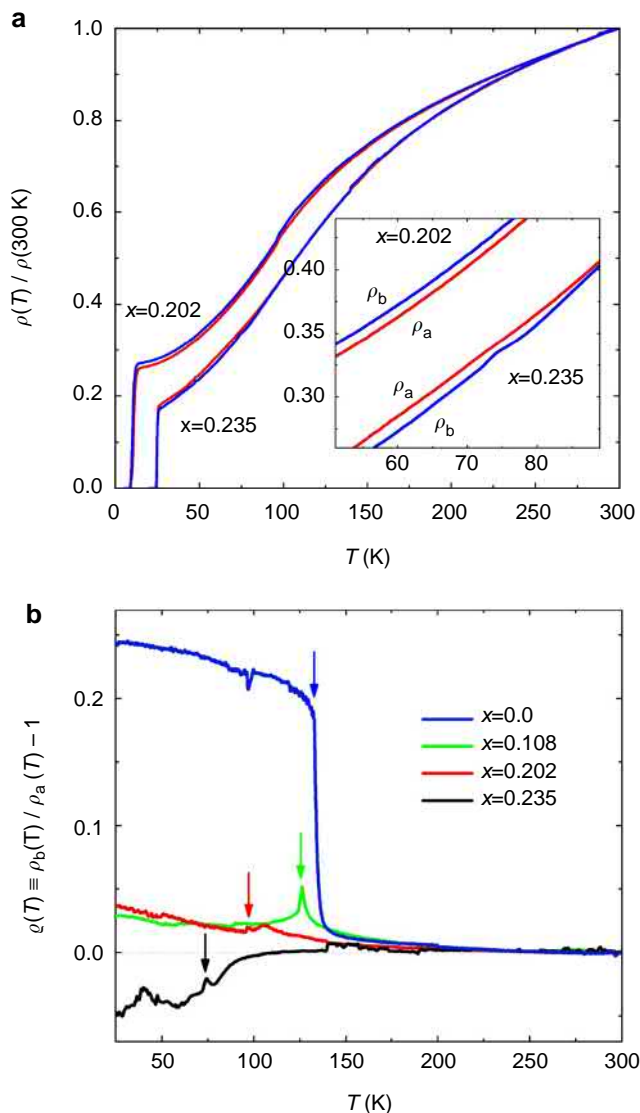


Figure 2 | Sign-change of the resistivity anisotropy. (a) Normalized temperature-dependent resistivity, $\rho(T)/\rho(300K)$, for the $(\text{Ba}_{1-x}\text{K}_x)\text{Fe}_2\text{As}_2$ samples with $x = 0.202$ and $x = 0.235$. The red lines show the resistivity along the a_0 -axis (ρ_a) while the blue lines show ρ_b . The inset zooms in on the structural transition, where a clear reversal of the anisotropy from $\rho_b > \rho_a$ for $x = 0.202$ to $\rho_b < \rho_a$ for $x = 0.235$ occurs. (b) Temperature dependence of ϱ for different K-doping levels. Arrows show T_N determined from $d\rho(T)/dT$ on unstrained samples.

doped compositions, but increases monotonically on cooling for higher hole doping levels. This signals that the low-temperature anisotropic reconstruction of the band structure due to long-range magnetic order has a progressively more important role near the hole-doped edge of the nematic/magnetic dome.

Electron versus hole doping. An interesting general picture emerges from the analysis of the experimental observations of this and previous studies^{20–22}. On the one hand, for all electron-doped $\text{Ba}(\text{Fe}_{1-x}\text{Co}_x)_2\text{As}_2$ and parent compositions, the resistivity anisotropy is positive, $\varrho(x) > 0$. The maximum anisotropy, $\varrho_{\text{max}}(x)$, shown in Fig. 1b, is peaked at some intermediate electron doping, vanishing near the edge of the magnetic/nematic dome, due to the vanishing orthorhombic distortion. On the other hand, on the hole-doped side, $\varrho_{\text{max}}(x)$ remains

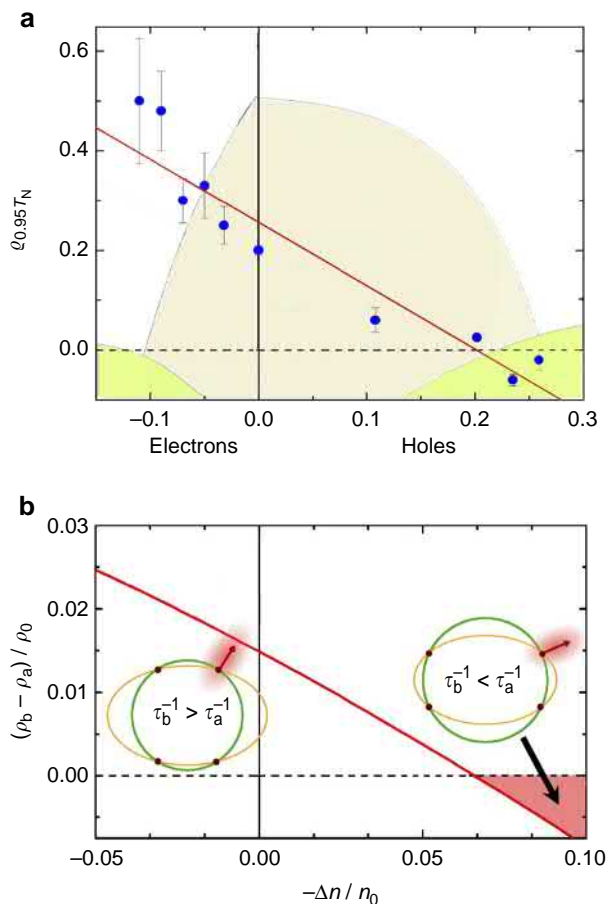


Figure 3 | Anisotropic scattering from spin fluctuations. (a) Doping dependence of the in-plane resistivity anisotropy at $0.95T_N$ in both electron- and hole-doped BaFe_2As_2 . The red line is a guide to the eye. The nematic/magnetic and superconducting domes are shown in the background for reference only, without a temperature scale. The error bars represent the values of the resistivity anisotropy ratio at T_N and reflect the uncertainty in the determination of T_N from the maximum of the $d\rho(T)/dT$ curves. (b) Theoretical calculation of the maximum in-plane resistivity anisotropy in the paramagnetic phase normalized by the residual resistivity, ρ_0 , as a function of the change in the electron occupation number, $\Delta n/n_0$, where $n_0 = (k_F a)^2/\pi$. The insets schematically show the differences in the scattering rates corresponding to different Fermi velocities at the hot-spots for electron- and hole-doped systems. When the hot-spot Fermi velocity has a larger component along the b (a) direction, the magnetic scattering rate is larger along the b (a) direction. The hot-spots are obtained by displacing the electron pocket (yellow ellipse) by $(\pi, 0)$, making it overlap with the hole pocket (green circle). The shaded red area denotes the predicted sign-reversal of the anisotropy.

positive up to moderate hole doping, but decreases by more than one order of magnitude, from $\varrho_{\text{max}}(x=0) \approx +0.3$ to $\varrho_{\text{max}}(x=0.202) \approx +0.02$. Even more surprisingly, $\varrho_{\text{max}}(x)$ changes sign and exhibits a minimum at a higher hole doping concentration, $\varrho_{\text{max}}(x=0.235) \approx -0.034$, before it eventually approaches zero close to the edge of the magnetic/nematic dome, near $x = 0.3$.

Discussion

Naively, the fact that $\rho_b > \rho_a$ across most of the phase diagram seems surprising, because the ferromagnetic direction appears to be less conducting than the antiferromagnetic one. From the

orbital ordering point of view^{11,24,25} one expects the opposite effect. However, a closer look at the Fermi surface reconstruction^{21,23} and the magnetic scattering mechanisms^{26,27} suggests that the anisotropy sign is decided by quantitative factors that depend on the electronic structure, going beyond general order parameter arguments. Moreover, the different contributions to the transport anisotropy do not necessarily compete with each other. To sort them out, we focus first on the nematic paramagnetic phase, in which scattering by magnetic fluctuations dominates and the band structure is not yet reconstructed by the magnetic order.

The experimental doping evolution of $\varrho(T \approx T_N)$, shown in Fig. 3a displays a rather monotonic behaviour, changing sign for sufficient hole-doping levels and vanishing at the edges of the nematic dome. Such a sign-change was previously predicted by the theoretical model of Fernandes *et al.*²⁶ for the anisotropic magnetic scattering in the nematic phase. The minimal model of Fernandes *et al.*²⁶, shown in the Supplementary Note 1 to be consistent with first-principles calculations, consists of a circular hole pocket at the center of the square-lattice Brillouin zone and two elliptical electron pockets centred at momenta $(\pi, 0)$ and $(0, \pi)$, which coincide with the magnetic-stripe ordering vectors (see Supplementary Figs S1 and S2). In the nematic phase, the amplitude of the fluctuations around these two ordering vectors becomes unequal¹², breaking the tetragonal symmetry of the system and inducing anisotropic scattering. In the experiment, the applied strain selects the $(\pi, 0)$ fluctuations.

The work by Fernandes *et al.*²⁶ showed that in the presence of impurities and in the low-temperature limit—but still in the paramagnetic phase—the scattering rates along a and b (and consequently the sign of the resistivity anisotropy) is controlled by the Fermi velocities of the hot-spots connecting the hole and electron pockets, see Fig. 3. Roughly in electron-doped compounds, the hot-spots Fermi velocity has a larger component along the b direction, giving rise to a larger scattering rate for electrons travelling along this direction, implying $\rho_b > \rho_a$. As the system is doped with holes, the hole pocket expands while the electron pocket shrinks, changing the position and the Fermi velocity of the hot-spots, which eventually acquires a larger component along the a direction, implying $\rho_a > \rho_b$. Although Fermi velocity measurements in detwinned hole-doped samples are not available, angle-resolved photoemission spectroscopy data in optimally Co-doped²⁸ and K-doped²⁹ twinned samples support such a change in the direction of the Fermi velocity at the hot-spots. The existence of hot-spots in optimally K-doped samples is also strongly supported by inelastic neutron scattering data, displaying overdamped-like behaviour in the normal state that disappears in the superconducting phase, where hot-spot electron states are gapped³⁰. To go beyond the low-temperature paramagnetic limit and make closer connection to the experiment, we used the same model of Fernandes *et al.*²⁶ and numerically obtained the maximum resistivity anisotropy in the paramagnetic phase as function of doping. The results, shown in Fig. 3b, agree qualitatively with the experimental data, capturing both the electron-hole asymmetry of $\varrho(T \approx T_N)$ and its sign-change in the hole-doped regime. This suggests that magnetic scattering has a central role in the paramagnetic phase.

Our data in Fig. 2 also show that the sign-change in the resistivity anisotropy persists down to $T = 0$, deep inside the magnetic state, where magnetic fluctuations are weaker. In this regime, transport should be governed by anisotropic reconstruction of the band structure. By employing first-principles calculations, we obtained the Fermi surface in the magnetically ordered state and evaluated ϱ in the relaxation-time approximation (see Supplementary Note 2).

Our calculations show that, in the parent compound, the reconstructed Fermi surface contains not only quasi-isotropic hole and electron pockets, but also Dirac cones whose crossing points are located slightly below the Fermi level (Supplementary Fig. S3). These features are in good agreement with quantum oscillation measurements²³. Owing to the large value of their Fermi velocities, these Dirac cones dominate the transport in the magnetic state, giving rise to an anisotropy in the resistivity that is in agreement with the experimental observations for $x = 0$. When holes are added to the system, the chemical potential shifts down, eventually crossing the Dirac points. Using the values extracted by angle-resolved photoemission spectroscopy^{31,32} and quantum oscillation measurements²³, we estimate this Dirac-point crossing to happen between 0.03 and 0.1 holes/Fe. For this doping concentration, the contribution to ϱ coming from the Dirac pockets is vanishingly small, making the contribution from the remaining pockets dominant (see Supplementary Figs S4 and S5). The latter depends on details that are beyond the accuracy of first-principles calculations, and can either yield a small positive or negative ϱ . Yet, our first-principles approach correctly captures the tendency of a vanishing ϱ inside the magnetically ordered phase in the hole-doped samples.

In conclusion, we observe the reversal of the in-plane resistivity anisotropy between electron- and hole-doped BaFe₂As₂ compounds. We attribute such behaviour to the spin-fluctuation scattering in the nematic phase and to the Dirac-cones contribution in the magnetically ordered phase. Both mechanisms complementarily predict a resistivity anisotropy that is larger in the electron-doped side and continuously smaller in the hole-doped side. We notice that other contributions not considered here, such as anisotropic impurity potential or anisotropic defects, can also affect the transport anisotropy in the iron pnictides. Our analysis offers an explanation for the change in the sign of the resistivity anisotropy in terms of the band structure of the pnictides, without invoking a change from itinerant to local moment physics, as suggested recently by Jiang *et al.*³³ Interestingly, the changes in the band structure from electron to hole-doped compounds^{34,35} also cause a reversal of the anisotropy in the magnetic correlation length³⁰, which, however, has little impact on the sign-changing of the resistivity anisotropy within our model²⁶. Besides shedding light on the singular character of the nematic phase in the iron pnictides, our observation serves as a unique fingerprint for the predominance of electronic scattering due to spin fluctuations, rather than phonons, in the normal state of these superconductors. Therefore, our study provides strong support to the concept that anomalous magnetic scattering in the proximity of a putative quantum critical point is intimately connected to magnetically mediated unconventional superconductivity^{36,37}.

Methods

Crystal growth and characterization. Single crystals of (Ba_{1-x}K_x)Fe₂As₂ with a size up to $7 \times 7 \times 1 \text{ mm}^3$ were grown from FeAs flux as described in Luo *et al.*³⁸ Potassium content in the samples was determined using electron probe microanalysis with wavelength dispersive spectroscopy, see Tanatar *et al.*³⁹ for details. Samples, had typical dimensions of 0.5 mm wide, 2–3 mm long and 0.05 mm thick, and were cut from cleaved slabs along the tetragonal [110] direction (which becomes either the orthorhombic a_0 or b_0 axis below T_{SM}). Optical imaging was performed on the samples while mounted on a cold finger in a continuous flow liquid helium cryostat (allowing for precise temperature control in 5 K to 300 K range) using a Leica DMLM microscope.

Polarized light microscopy was used for visualization of the structural domains¹⁷ and the sample selection was based on the clarity of domains in the image. In Fig. 4, we show polarized light images of the area between potential contacts in (Ba_{1-x}K_x)Fe₂As₂ crystals used in this study, with $x = 0.108$ (non-superconducting), $x = 0.202$ ($T_c = 10 \text{ K}$), $x = 0.235$ ($T_c = 26 \text{ K}$) and $x = 0.259$ ($T_c = 28 \text{ K}$). Images were taken on cooling at a temperature slightly above T_c and at base temperature. The highest contrast is observed when the sample is aligned with the [100] tetragonal direction at a 45° to the polarization direction

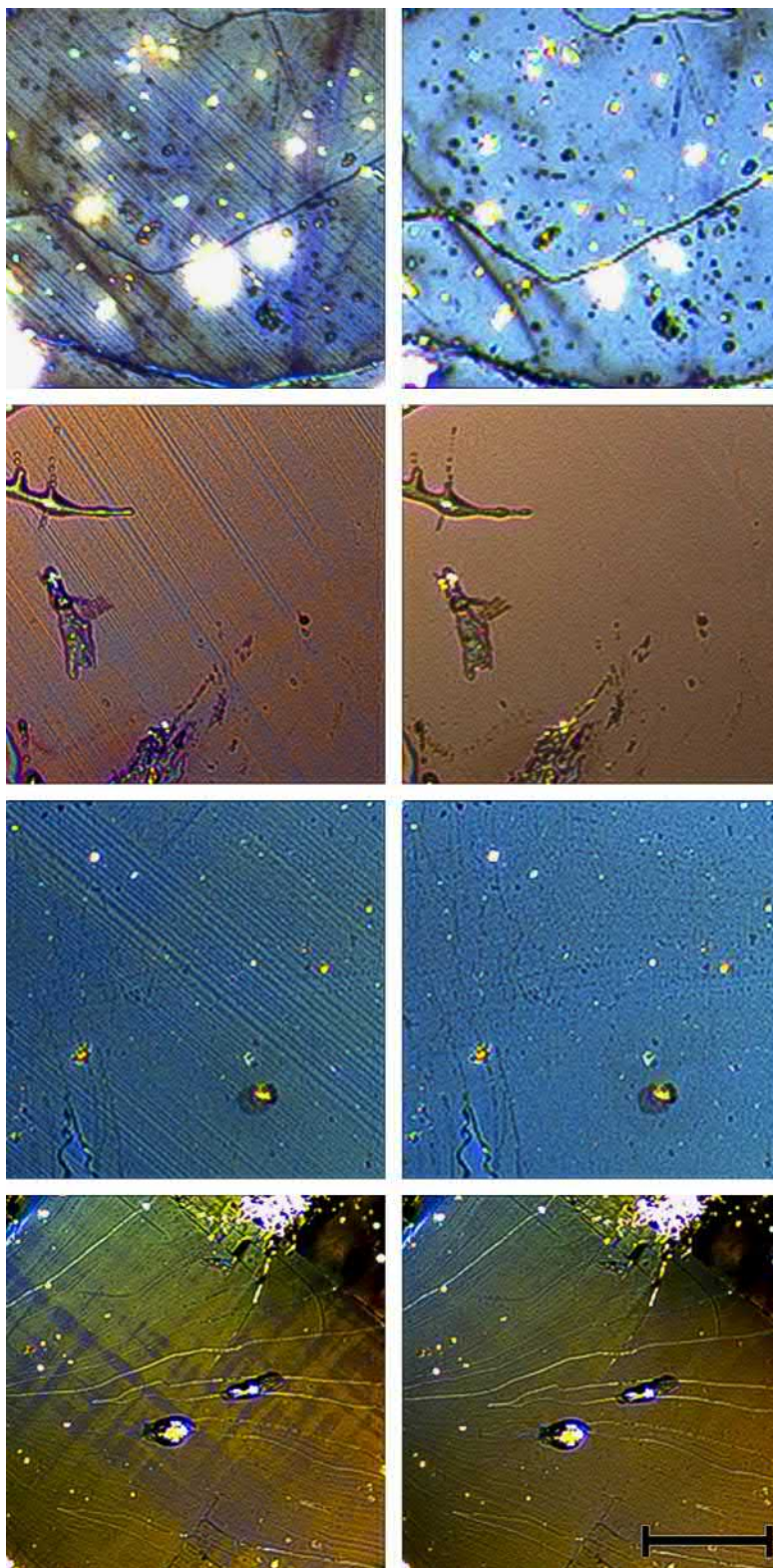


Figure 4 | Visualization of structural domains. Polarized light microscopy of $(\text{Ba}_{1-x}\text{K}_x)\text{Fe}_2\text{As}_2$ samples with doping levels $x = 0.108, 0.202, 0.235, 0.259$, from top to bottom. Images were taken at temperatures just above the tetragonal-to-orthorhombic structural transition ($T > T_S$, right) and 5 K ($T < T_S$, left), the latter showing formation of structural domains due to four different orientations of a_0 and b_0 axes. The difference in colour of the domains is due to spectral dependence of bireflectance, depending on angle between the a_0 direction and the polarization plane of incident white light. As bireflectance is proportional to the orthorhombic distortion, the contrast naturally vanishes in the tetragonal phase (right panels). Scale bar, 100 μm .

of incident light (parallel and perpendicular to the orthorhombic a_0 in different domains). The contrast of domain images depends on the quality of the surface and the homogeneity of the samples. Domains are observed for samples

with $x \approx 0.26$, and are no longer observed for samples with a higher doping level, $x = 0.34$, which also do not show any features associated with a structural transition in $\rho(T)$.

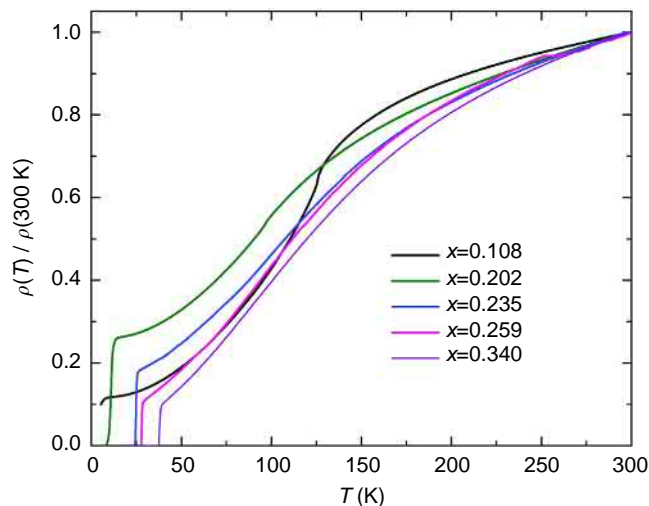


Figure 5 | Temperature-dependent resistivity. Temperature-dependent resistivity along the orthorhombic a_0 -axis, ρ_a for samples of $(\text{Ba}_{1-x}\text{K}_x)\text{Fe}_2\text{As}_2$ with four different potassium doping levels in the strain-free, twinned state. The curves are shown using normalized plots, $\rho(T)/\rho(300\text{ K})$.

Resistivity measurements and mechanical detwinning. Selected samples were mounted for four-probe electrical resistivity measurements, with contacts made by soldering 50 μm Ag wires using low-resistance Sn soldered contacts⁴⁰. Initial resistivity measurements on each sample were carried out using a flexible wire arrangement with no strain applied to the sample (free standing state). The results are plotted in Fig. 5. As this measurement is performed in the twinned state of the sample and contains contributions from both components of the in-plane resistivity in the orthorhombic phase, we call it ρ_t . Samples were then mounted on a brass horseshoe straining device, and strain was applied through the voltage contact wires by deformation of the horseshoe, see Tanatar *et al.*²¹ and Blomberg *et al.*⁴¹ for the details of the procedure. Strain in this configuration is applied along the tetragonal [110] axis, which selects the orthorhombic a_0 -axis as a preferable direction upon cooling below T_S . Very soft current leads apply no strain. The strain was incrementally increased, and for each increment, temperature-dependent resistivity measurements were made and the domain structure was imaged to determine the completeness of detwinning. Our previous studies^{18,21} using x-ray scattering have shown that when crystals are strained to the point at which no domains are visible in polarized microscopy, about 90% of the whole bulk of the sample represents the domain whose orthorhombic a_0 -axis is oriented along the direction of the strain and, therefore, parallel to the current. Therefore, in the detwinned state we are predominantly measuring the a_0 -axis resistivity, ρ_a , while in the unstrained state of the sample roughly equal contributions of both resistivity components are measured. Therefore, we may calculate the b_0 axis resistivity, $\rho_b(T) = 2\rho_t(T) - \rho_a(T)$.

References

- Paglione, J. & Greene, R. L. High-temperature superconductivity in iron-based materials. *Nat. Phys.* **6**, 645–658 (2010).
- Johnston, D. C. The puzzle of high temperature superconductivity in layered iron pnictides and chalcogenides. *Adv. Phys.* **59**, 803–1061 (2010).
- de la Cruz, C. *et al.* Magnetic order close to superconductivity in the iron-based layered $\text{LaO}_{1-x}\text{F}_x\text{FeAs}$ systems. *Nature* **453**, 899–902 (2008).
- Fisher, I. R., Degiorgi, L. & Shen, Z. X. In-plane electronic anisotropy of underdoped ‘122’ Fe-arsenide superconductors revealed by measurements of detwinned single crystals. *Rep. Prog. Phys.* **74**, 124506 (2011).
- Yi, M. *et al.* Symmetry-breaking orbital anisotropy observed for detwinned $\text{Ba}(\text{Fe}_{1-x}\text{Co}_x)_2\text{As}_2$ above the spin density wave transition. *Proc. Natl Acad. Sci.* **108**, 6878–6883 (2011).
- Kasahara, S. *et al.* Electronic nematicity above the structural and superconducting transition in $\text{BaFe}_2(\text{As}_{1-x}\text{P}_x)_2$. *Nature* **486**, 382–385 (2012).
- Chu, J.-H., Kuo, H.-H., Analytis, J. G. & Fisher, I. R. Divergent nematic susceptibility in an iron arsenide superconductor. *Science* **337**, 710712 (2012).
- Fang, C., Yao, H., Tsai, W.-F., Hu, J. & Kivelson, S. A. Theory of electron nematic order in LaFeAsO . *Phys. Rev. B* **77**, 224509 (2008).
- Xu, C., Muller, M. & Sachdev, S. Ising and spin orders in the iron-based superconductors. *Phys. Rev. B* **78**, 020501(R) (2008).
- Mazin, I. I. & Johannes, M. D. A key role for unusual spin dynamics in ferropnictides. *Nat. Phys.* **5**, 141–145 (2009).
- Valenzuela, B., Bascones, E. & Caldern, M. J. Conductivity anisotropy in the magnetic state of iron pnictides. *Phys. Rev. Lett.* **105**, 207202 (2010).
- Fernandes, R. M., Chubukov, A. V., Knolle, J., Eremin, I. & Schmalian, J. Preemptive nematic order, pseudogap, and orbital order in the iron pnictides. *Phys. Rev. B* **85**, 024534 (2012).
- Kivelson, S. A., Fradkin, E. & Emery, V. J. Electronic liquid-crystal phases of a doped Mott insulator. *Nature* **393**, 550–553 (1998).
- Cooper, K. B., Lilly, M. P., Eisenstein, J. P., Pfeiffer, L. N. & West, K. W. Onset of anisotropic transport of two-dimensional electrons in high Landau levels: Possible isotropic-to-nematic liquid-crystal phase transition. *Phys. Rev. B* **65**, 241313(R) (2002).
- Borzi, R. A. *et al.* Formation of a nematic fluid at high fields in $\text{Sr}_3\text{Ru}_2\text{O}_7$. *Science* **315**, 214–217 (2006).
- Lawler, M. J. *et al.* Intra-unit-cell electronic nematicity of the high- T_c copper-oxide pseudogap states. *Nature* **466**, 347–351 (2010).
- Tanatar, M. A. *et al.* Direct imaging of the structural domains in the iron pnictides AFe_2As_2 ($\text{A} = \text{Ca}, \text{Sr}, \text{Ba}$). *Phys. Rev. B* **79**, 180508 (2009).
- Blomberg, E. C. *et al.* Effect of tensile stress on the in-plane resistivity anisotropy in BaFe_2As_2 . *Phys. Rev. B* **85**, 144509 (2012).
- Fernandes, R. M. *et al.* Effects of nematic fluctuations on the elastic properties of iron arsenide superconductors. *Phys. Rev. Lett.* **105**, 157003 (2010).
- Chu, J.-H. *et al.* In-plane resistivity anisotropy in an underdoped iron arsenide superconductor. *Science* **329**, 824–826 (2010).
- Tanatar, M. A. *et al.* Uniaxial-strain mechanical detwinning of CaFe_2As_2 and BaFe_2As_2 crystals: Optical and transport study. *Phys. Rev. B* **81**, 184508 (2010).
- Ying, J. J. *et al.* Measurements of the anisotropic in-plane resistivity of underdoped FeAs-based pnictide superconductors. *Phys. Rev. Lett.* **107**, 067001 (2011).
- Terashima, T. *et al.* Complete fermi surface in BaFe_2As_2 observed via Shubnikov-de Haas oscillation measurements on detwinned single crystals. *Phys. Rev. Lett.* **107**, 176402 (2011).
- Chen, C.-C., Maciejko, J., Sorini, A. P., Moritz, B., Singh, R. R. P. & Devereaux, T. P. Orbital order and spontaneous orthorhombicity in iron pnictides. *Phys. Rev. B* **82**, 100504 (2010).
- Lv, W. & Phillips, P. Orbital and magnetically induced anisotropy in iron-based superconductors. *Phys. Rev. B* **84**, 174512 (2011).
- Fernandes, R. M., Abrahams, E. & Schmalian, J. Anisotropic in-plane resistivity in the nematic phase of the iron pnictides. *Phys. Rev. Lett.* **107**, 217002 (2011).
- Liang, S., Alvarez, G., Sen, C., Moreo, A. & Dagotto, E. Anisotropy of electrical transport in pnictide superconductors studied using Monte Carlo simulations of the spin-fermion model. *Phys. Rev. Lett.* **109**, 047001 (2012).
- Liu, C. *et al.* Evidence for a Lifshitz transition in electron-doped iron arsenic superconductors at the onset of superconductivity. *Nat. Phys.* **6**, 419–423 (2010).
- Ding, H. *et al.* Electronic structure of optimally doped pnictide $\text{Ba}_{0.6}\text{K}_{0.4}\text{Fe}_2\text{As}_2$: a comprehensive angle-resolved photoemission spectroscopy investigation. *J. Phys. Condens. Matt.* **23**, 135701 (2011).
- Zhang, C. *et al.* Neutron scattering studies of spin excitations in hole-doped $\text{Ba}_{0.67}\text{K}_{0.33}\text{Fe}_2\text{As}_2$ superconductor. *Sci. Rep.* **1**, 115 (2011).
- Shimojima, T. *et al.* Orbital-dependent modifications of electronic structure across the magnetostructural transition in BaFe_2As_2 . *Phys. Rev. Lett.* **104**, 057002 (2010).
- Kim, Yeongkwan *et al.* Electronic structure of detwinned BaFe_2As_2 from photoemission and first principles. *Phys. Rev. B* **83**, 064509 (2011).
- Jiang, Juan *et al.* The distinct in-plane resistivity anisotropy in the nematic states of detwinned NaFeAs and FeTe single crystals: evidences for Hund’s rule metal. Preprint at <http://arxiv.org/abs/1210.0397> (2012).
- Zhang, J., Sknepnek, R. & Schmalian, J. Spectral analysis for the iron-based superconductors: Anisotropic spin fluctuations and fully gapped s^{+-} -wave superconductivity. *Phys. Rev. B* **82**, 134527 (2010).
- Park, J. T. *et al.* Symmetry of spin excitation spectra in the tetragonal paramagnetic and superconducting phases of 122-ferropnictides. *Phys. Rev. B* **82**, 134503 (2010).
- Mathur, N. D. *et al.* Magnetically mediated superconductivity in heavy fermion compounds. *Nature* **394**, 39–43 (1998).
- Taillefer, L. Scattering and pairing in cuprate superconductors. *Annu. Rev. Condens. Matt. Phys.* **1**, 51–70 (2010).
- Luo, H. Q., Wang, Z. S., Yang, H., Cheng, P., Zhu, X. & Wen, H.-H. Growth and characterization of $\text{A}_{1-x}\text{K}_x\text{Fe}_2\text{As}_2$ ($\text{A} = \text{Ba}, \text{Sr}$) single crystals with $x = 0-0.4$. *Supercond. Sci. Technol.* **21**, 125014 (2008).
- Tanatar, M. A. *et al.* Anisotropic resistivity in underdoped single crystals $(\text{Ba}_{1-x}\text{K}_x)\text{Fe}_2\text{As}_2$, $0 \leq x < 0.35$. Preprint at <http://arxiv.org/abs/1106.0533> (2011).
- Tanatar, M. A., Ni, N., Bud’ko, S. L., Canfield, P. C. & Prozorov, R. Field-dependent transport critical current in single crystals of $\text{Ba}(\text{Fe}_{1-x}\text{TM}_x)_2\text{As}_2$ ($\text{TM} = \text{Co}, \text{Ni}$) superconductor. *Supercond. Sci. Technol.* **23**, 054002 (2010).

41. Blomberg, E. C. *et al.* In-plane anisotropy of electrical resistivity in strain-detwinned SrFe₂As₂. *Phys. Rev. B* **83**, 134505 (2011).

Acknowledgements

We thank A.V. Chubukov for useful comments, suggestions and critical reading of the manuscript. R.M.F. and J.S. acknowledge useful discussions with E. Abrahams. Work at The Ames Laboratory was supported by the US Department of Energy, Office of Basic Energy Sciences, Division of Materials Sciences and Engineering under contract no. DE-AC02-07CH11358. The work in China was supported by the NSF of China, the Ministry of Science and Technology of China (973 projects: 2011CBA00102, 2012CB821403). R.M.F. acknowledges the support of the NSF Partnerships for International Research and Education (PIRE) programme OISE-0968226.

Author contributions

R.P. and M.A.T. conceived and designed the project. M.A.T., R.P. and E.C.B. developed the detwinning technique and performed transport measurements. E.C.B. performed

optical measurements. R.M.F., I.I.M., J.S., and M.D.J. carried out theoretical modelling and calculations. B.S. and H.-H.W. grew the single crystals and performed their characterization. M.A.T., R.P., R.M.F., E.C.B., and I.I.M. wrote the manuscript with input from all authors.

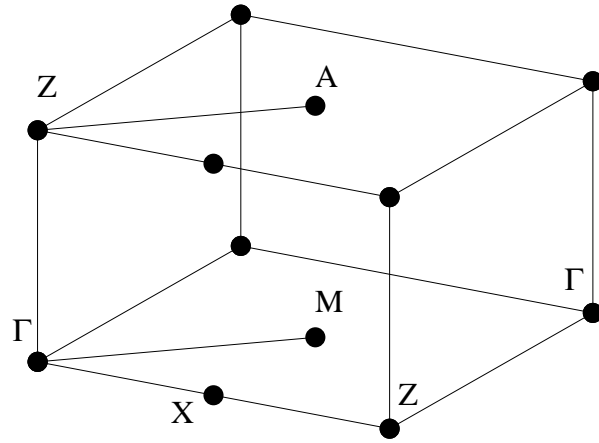
Additional information

Supplementary Information accompanies this paper at <http://www.nature.com/naturecommunications>

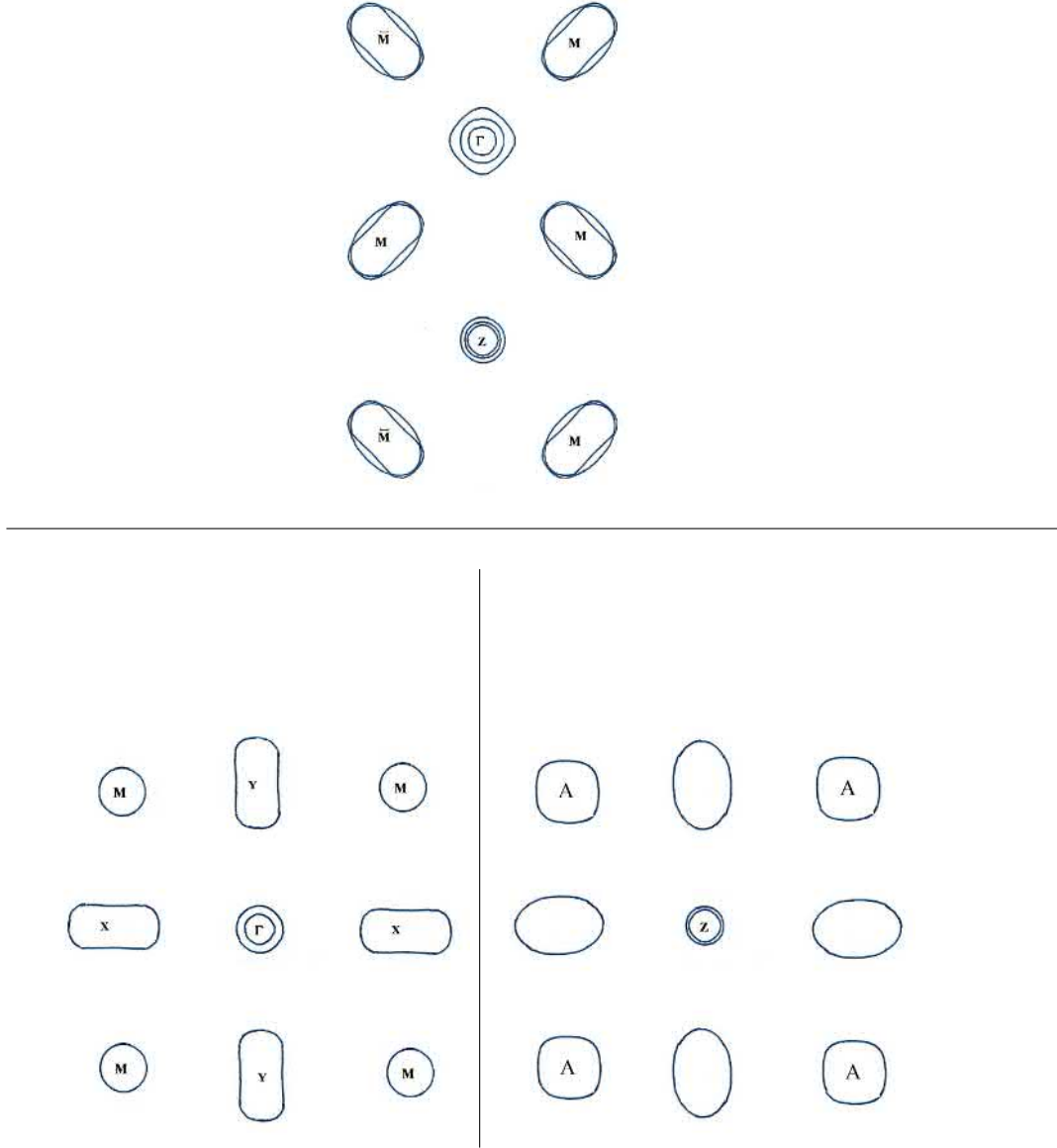
Competing financial interests: The authors declare no competing financial interests.

Reprints and permission information is available online at <http://npg.nature.com/reprintsandpermissions/>

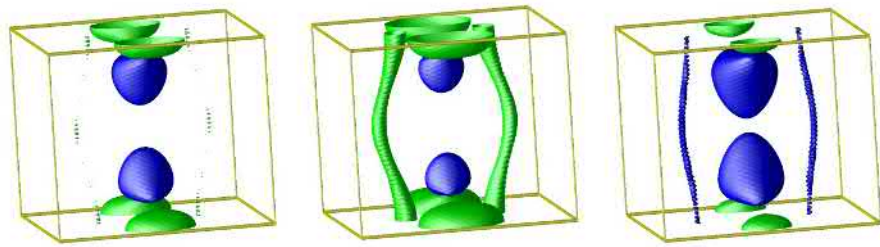
How to cite this article: Blomberg, E. C. *et al.* Sign-reversal of the in-plane resistivity anisotropy in hole-doped iron pnictides. *Nat. Commun.* 4:1914 doi: 10.1038/ncomms2933 (2013).



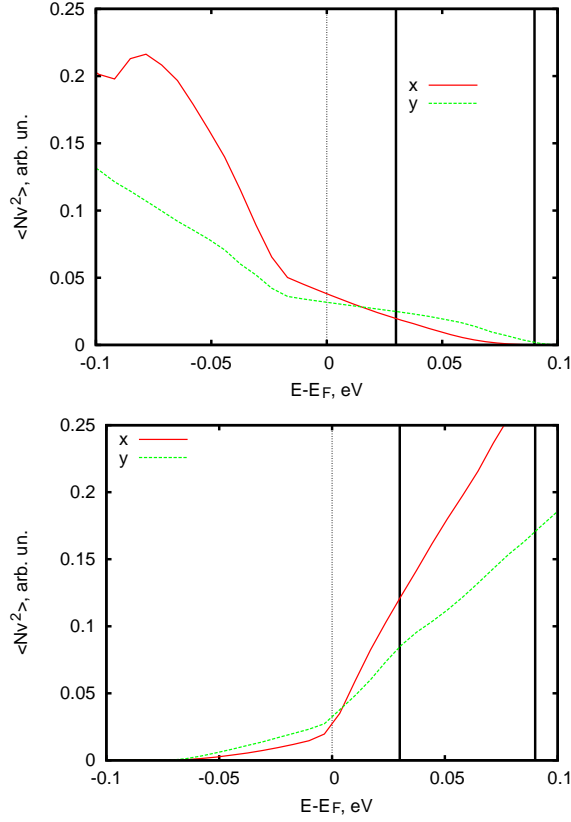
Supplementary Figure S1: **The Brillouin zone of BaFe₂As₂.** The Brillouin zone of BaFe₂As₂ corresponding to the two Fe unit cell.



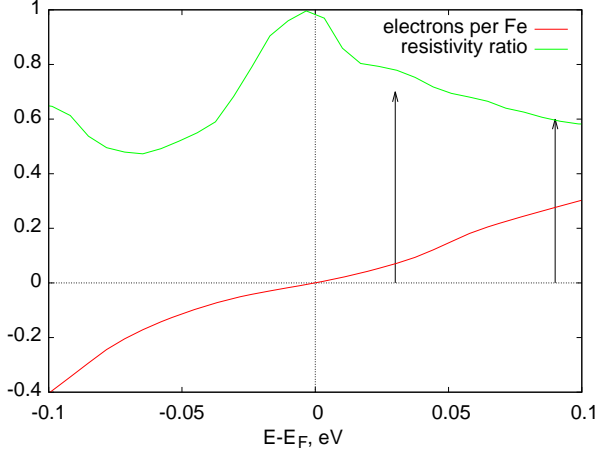
Supplementary Figure S2: **Fermi surfaces of BaFe_2As_2** . Upper panel: First-principles calculated Fermi surface cross-sections for Ba122 in the folded Brillouin zone. Lower panels: the Fermi surface obtained from the unfolding procedure discussed in the text across $k_z = 0$ (left panel) and $k_z = \pi$ (right panel).



Supplementary Figure S3: **Fermi surface deep inside magnetically ordered state.** The Fermi surface calculated deep inside the magnetically ordered phase for parent (left panel) electron- (middle panel) and hole - doped (right panel) compositions. Green - electron pockets, blue - hole pockets.



Supplementary Figure S4: **Calculated transport functions.** Calculated transport functions, $\langle Nv_F^2 \rangle$, for holes and electrons. The two bold vertical lines correspond to the minimal and maximal estimates of the shift of the chemical potential, required to adjust the calculations to the experiment, as discussed in the text. Note two different regimes, when Dirac cones are present, and where they are not.



Supplementary Figure S5: **Calculated resistivity anisotropy.** The hole per Fe filling factor (lower curve) and the resistivity ratio, ρ_a/ρ_b (upper curve) obtained using band structure calculation, as described in the text. Note that the “as-calculated” Dirac points lie precisely on the Fermi level, and the resistivity anisotropy is essentially zero. In order to match the calculated Fermi surfaces with ARPES and quantum-oscillation experiments, respectively [31,32,23], one needs to shift the calculated Fermi level of BaFe₂As₂, correspondingly, by 30 meV and 90 meV shifts. The resulting positions are indicated by arrows. After these shifts are applied, the minimal anisotropy ($\rho_a/\rho_b \approx 1$) appear at the left of the arrows, that is to say, in the hole doping regime. Note that no symmetry demands that ρ_a/ρ_b be less than 1, small variation in the calculated band structure could render it slightly larger than 1, as observed in the experiment.

Supplementary Note 1: Contribution of the spin-fluctuation scattering

To justify the minimal model developed in Ref.[26], and used here to calculate the resistivity anisotropy shown in Fig. 3 of the main text, we use first-principles band structure calculations. The first step is to unfold the first-principles Fermi surface from the two-Fe unit cell to an effective one-Fe unit cell, where the two magnetic ordering vectors are given by $\mathbf{Q}_1 = (\pi, 0)$ and $\mathbf{Q}_2 = (0, \pi)$. In the Ba122 system, due to a sizeable hybridization with the As orbitals, there are two ways to unfold the overlapping and hybridized electron bands. One consists of constructing Wannier functions from a particular energy window (usually near the Fermi surface), symmetrizing them according to the primitive tetragonal group, and recalculating the band structure using the obtained Wannier functions [42]. This method provides a reasonable agreement of the folded bands with full DFT calculations, but this agreement may be achieved not through an appropriate As-induced hybridization, but through unphysically large one-electron hopping. The other method makes use of the actual symmetry element that reduces the larger unit cell to a smaller one: a glide plane. This method has been discussed in details in Ref. [43], and more briefly in Ref. [44]. It is this unfolding procedure that is appropriate for our purposes.

In the upper panel of Fig. S2 we show the DFT-calculated Fermi surface cross-sections by the plane $k_z = 0$. Because of the body-centered symmetry the point $Z = (0, 0, \pi)$ is equivalent to $(2\pi, 0, 0)$ (see Fig. 1 for notations). Therefore, the ellipticities of the electron pockets with respect to the point Z are opposite to those with respect to the point Γ . In the lower panel of Fig. S2 we show the Fermi surface cross-sections in the unfolded band from which the Fermi surface of the upper panel originates. In the unfolded zone, the ellipticity of the electron pockets with respect to Z is the same as with respect to Γ , but opposite as compared to the eccentricity with respect to M and A (see the notation in Fig. S1). After folding, the point M folds upon Z , and point A upon Γ , thus creating an impression that the ellipticity changes sign with k_z .

We note that there are two hole pockets at ΓZ but only one at MA , indicating that the dominating scattering processes are between the hole pockets at ΓZ and the electron pockets. This shows that the model of Ref.[26], considering a two-dimensional three band model with a circular hole pocket at the center Γ of the unfolded Brillouin zone and two elliptical electron pockets located at $X = (\pi, 0)$ and $Y = (0, \pi)$, is an appropriate starting point. Within this model, the conductivity tensor is given by:

$$\sigma_{ij} = -e \sum_{\mathbf{k}, \lambda} v_{\mathbf{k}, \lambda}^i f_{\mathbf{k}, \lambda}^j$$

where $v_{\mathbf{k}, \lambda}^i = \partial \varepsilon_{\mathbf{k}, \lambda} / \partial k_i$ is the component i of the Fermi velocity of band λ and $f_{\mathbf{k}, \lambda}^j$ is the non-equilibrium electronic distribution function for a (unit) electric field applied along the j direction. The latter can be obtained by solving the Boltzmann equation in the presence of scattering by impurities and spin fluctuations, as explained in details in Ref.[26]. To obtain the results of Fig. 3, we followed the approach of Ref.[26], considering a putative magnetic quantum critical point and numerically calculating the temperature-dependent resistivity anisotropy. We used the same parameters as those of Ref.[26], varying the chemical potential to mimic the effects of hole doping and electron doping. For each value of the chemical potential, we obtained the complete temperature-dependence of the paramagnetic resistivity anisotropy and then extracted the maximum anisotropy, obtaining the results of Fig. 3.

Supplementary Note 2: Contribution of the Dirac cones: first-principles calculations

In order to address the kinematic effect of the magnetically-reconstructed Fermi surface anisotropy, we calculated the transport anisotropy using the actual DFT band structure and the constant relaxation time approximation. It has been established that GGA calculations, even though they overestimate the long-range ordered magnetic moment by about a factor of two, provide a better agreement with the experimental Fermi surface than DMFT calculations, which yield the correct magnetic moment [23]. This is, incidentally, another manifestation that not only the local fluctuations, accounted for in DMFT, but also nematic fluctuations, consistent with a short range magnetic order of several lattice parameters, are responsible for the reduction of the ordered moment [10]. With this in mind, we used full potential LAPW bands, with full GGA magnetization, including spin-orbit interaction, to compute the Fermi surfaces and the Fermi velocities.

The Fermi surface calculated deep inside the magnetically ordered phase of the parent compound, shown in the left panel of Fig. S3, displays two sets of quasi-isotropic pockets: one for the holes (blue) and one for the electrons (green). It also displays barely visible threads, corresponding to the Dirac cones. They are green, indicating that in the calculations the Dirac points are located very slightly below, but practically at the Fermi

level. Shifting the Fermi level up by 30 meV transforms the Dirac pockets into clearly visible electron tubes (middle panel in Fig. S3), while moving it down (right panel in Fig. S3) creates hole tubes instead. As pointed out in Ref. [45], the Fermi velocity in the Dirac cones is high, therefore whenever they are present, they dominate the transport. Near the Dirac point, the contribution from a Dirac cone to transport is $Nv_F^2 \propto |E|$, where E is the energy distance from the Dirac point.

Using an extra-fine mesh of about 60000 inequivalent k-points (44x44x40 divisions in the full Brillouin zone) we have calculated the transport function $Nv_F^2(E)$ as a function of energy, separately for the hole bands and electron bands (Fig. 4). One can see very clearly two regimes: one, where both regular and Dirac electrons contribute, and the other, where the latter contribution disappears. Except very near the Dirac point itself, Dirac electrons dominate transport. This is easy to understand: electronic transport, for a given scattering rate, is defined by the product of the density of states and squared Fermi velocity. For parabolic 2D bands this product is proportional to n (where n is the number of electrons in the pocket), but for linear (Dirac) bands to \sqrt{n} . Thus, when the small (“Dirac”) pockets are present they dominate the transport, and they happen to have a particular anisotropy (although this purely accidental and may be different in a different compounds), which is the anisotropy we observe experimentally at zero doping. Upon the hole doping, these pockets disappear, and the observed anisotropy is now defined by the larger Fermi surfaces, which in our calculations appears to be zero, but given the uncertainty of the DFT could as well be finite, but small, and have the opposite sign (there is no general argument setting this sign, it is purely accidental).

Moreover, contrary to the assumption in Ref. [45], the anisotropy comes mostly from the Dirac cones, and not from the “round” pockets. As Fig. S5 shows, the total anisotropy is vanishingly small when the Fermi level crosses the Dirac cones right at the Dirac point, which happens for $E \approx E_F$ in the calculation. Away from this chemical potential, the anisotropy grows, retaining its positive value $\rho_b/\rho_a > 1$, for either hole or electron doping away from this point.

In the calculation, the Dirac point is very near the Fermi level for the undoped compound. To determine where it is in the real material, we can use the ARPES data of Ref. [31,32], or preferably, the quantum oscillation measurements of Ref. [23]. In the latter work, the authors observe that in order to bring the Dirac cone area into complete agreement with the experiment, they need to shift the Fermi level in their LDA calculations up by 30 meV. In the former work, it was observed that the Dirac points are located

30 meV below the actual Fermi level. At the same time, they observed a factor of about three in the effective mass renormalization, implying that, in the unrenormalized band structure, the corresponding shift of the Fermi level would be 90 meV.

One could actually restrict the integration to particular parts of the Brillouin zone and separate the Dirac contribution from the rest. After that, one could shift the Dirac bands by the amount suggested by the experiment, and the other bands by their measured shift. This is however unnecessary, because the anisotropy is dominated by the Dirac band (Fig. S4), and shifts of the other bands do not really matter. Therefore, we calculated the total anisotropy as a function of doping, using straight DFT band structure, and simply marked (Fig. S5) the position of the Fermi level of the parent compound corresponding to the aforementioned 30 meV and 90 meV shifts. As mentioned, the minimal anisotropy, which corresponds to 0.03-0.1 h/Fe , depending on the shift, is nearly zero, but this is accidental; it could be a small positive or a small negative number (as in the experiment). DFT certainly does not describe these compounds at the level of accuracy sufficient to distinguish between these possibilities. Yet, it consistently describes the vanishing resistivity anisotropy in the magnetically ordered phase as holes are doped into the system.

Supplementary References

- [42] S. Graser, A. F. Kemper, T. A. Maier, H.-P. Cheng, P. J. Hirschfeld, and D. J. Scalapino. Spin fluctuations and superconductivity in a three-dimensional tight-binding model for BaFe₂As₂. Phys. Rev. B **81**, 214503 (2010).
- [43] O.K. Andersen, L. Boeri. On the multi-orbital band structure and itinerant magnetism of iron-based superconductors. Annalen der Physik, **1**, 8-50 (2011).
- [44] P.J. Hirschfeld, M.M. Korshunov, I.I. Mazin. Gap symmetry and structure of Fe-based superconductors. Reports on Progress in Physics **74**, 124508 (2011).
- [45] H.-H. Kuo, J.-H. Chu, S. C. Riggs, L. Yu, P. L. McMahon, K. De Greve, Y. Yamamoto, J. G. Analytis and I. R. Fisher. Possible origin of the nonmonotonic doping dependence of the in-plane resistivity anisotropy of Ba(Fe_{1-x}T_x)₂As₂ (T=Co, Ni and Cu). Phys. Rev. B **84**, 054540 (2011).